Structural, catalytic/redox and electrical characterization of systems combining Cu–Ni with CeO$_2$ or Ce$_{1-x}$M$_x$O$_{2-\delta}$ (M = Gd or Tb) for direct methane oxidation

A. Hornés[a], D. Gamarra[a], G. Munuera[b], A. Fuerte[c], R.X. Valenzuela[c], M.J. Escudero[c], L. Daza[a,c], J.C. Conesa[a], P. Bera[a], A. Martínez-Arias[a,*]

[a] Instituto de Catálisis y Petroleoquímica (CSIC), C/Marie Curie 2, Campus de Cantoblanco, 28049 Madrid, Spain
[b] Universidad de Sevilla, C/Profesor García González s/n, Departamento de Química Inorgánica, 41012 Sevilla, Spain
[c] CIEMAT, Avda, Complutense 22, 28040 Madrid, Spain

ABSTRACT

The present work analyses bimetallic Cu–Ni formulations, in comparison to monometallic Cu ones, combined with CeO$_2$ or other structurally related mixed oxides resulting from doping of the former with Gd or Tb, focusing to its possible use as anodes of solid oxide fuel cells (SOFC) for direct oxidation of methane. The main objective is the characterization of the various formulations at structural level as well as with regards to the redox changes taking place in the systems upon interaction with methane, in order to evaluate the effects induced by the presence of dopants. In the same sense, an analysis of thermal expansion and electrical properties of the systems is performed, considering its possible implantation in SOFC single cells. For the mentioned purposes, the systems have been analysed by means of CH$_4$-TPR tests subsequently followed by TPO tests, as well as by XRD, Raman and XPS, with the aim of exploring structural and redox changes produced in the systems and the formation of carbon deposits during such interactions. The results reveal significant modifications in the structural, catalytic/redox and electrical properties of the systems as a function of the presence of Ni and/or Gd and Tb dopants in the formulation.

© 2008 Elsevier B.V. All rights reserved.

1. Introduction

Solid oxide fuel cells (SOFC) are galvanic devices most interesting from environmental and energetic points of view due to their high efficiency for conversion from chemical to electrical energy and their high versatility towards employment of various types of fuels [1]. Classical systems of this type involve the employment of thin YSZ electrolytes with an anode typically based on Ni–YSZ cermets and can attain an energetic efficiency close to 70% operating at relatively high temperature (800–1000 °C) with hydrocarbon reforming mixtures as fuel [1–3]. This efficiency can be theoretically increased by employing direct hydrocarbon oxidation conditions instead of fuel mixtures resulting from reforming [4]. However, the classical anode of nickel could easily be deactivated under those conditions as a consequence of the formation of carbonaceous deposits due to the relatively good activity of nickel for hydrocarbon cracking [5–8]. Different alternatives were developed in this respect to overcome such deactivating effect. Murray et al. [6] successfully operated a cell on dry methane by employing a nickel-containing ceria-based anode at relatively low reaction temperature (650 °C). In turn, such ceria-containing anode could in principle be compatible with electrolytes able to operate at intermediate temperatures (500–700 °C) like gadolinium-doped ceria (CGO) [1].

However, the nickel-based anode can be less suitable when less refractory, more easy to be cracked hydrocarbons are employed as fuel [5,7,8]. A more versatile alternative was developed by Gorte and co-workers and consisted in employing anodes including mixtures between copper and cerium oxide [5,7,9–16]. Such configuration has demonstrated to be able to employ a large diversity of hydrocarbon fuels (methane or longer chain ones and even aromatics) under direct oxidation conditions and displaying a reasonable stability [4,7,11]. However, although it could in principle perform well at intermediate temperatures, the copper anode can present several limitations related to its relatively low melting temperature, which can make difficult the fabrication of Cu cermets and affect the anode stability when operating at high temperature [16,17], as well as to its poor performance for hydrocarbon activation [4,16]. An interesting alternative in this sense consists in employing bi- or multi-metallic anode formulations [4,18,19].

In this context, the present work explores the properties of bimetallic Cu–Ni configurations, considering the higher thermal stabilities and chemical reactivity of nickel with respect to copper, for direct methane oxidation, using a basic copper-ceria configuration as the starting reference material. The effects of the modifications of the properties of ceria that occur upon doping with

* Corresponding author. Tel.: +34 915854940; fax: +34 915854760.
 E-mail address: amartinez@icp.csic.es (A. Martínez-Arias).

Gd and Tb [20] are also analysed; in this respect, previous work of our group demonstrated that doping of ceria with Tb induces changes in the type of conductivity and makes the system somewhat more stable towards thermal sintering [21]. The work extends the results of a previous analysis of catalytic properties of this type of systems for methane direct oxidation [22], paying in this case particular attention to characterization of their structural, catalytic/redox and electrical properties. For this purpose, materials synthesized by a microemulsion method were examined by XRD, XPS and S_{BET} and analysed with respect to their redox/catalytic properties by means of TPR tests under dry methane; supplementary analysis of thermal expansion coefficient and electrical conductivity both under air or diluted H_2 is also provided. The work will explore also with TPO, Raman and XPS the generation of carbon deposits during direct hydrocarbon interaction and the chemical changes produced by them on the composite material; these are expected to affect the anode components and the SOFC performance. In general, such deposits will poison the anode, although in some bimetallic Cu–M configurations they have displayed positive effects attributed to an increase of electrical conduction that would be due to an enhanced connectivity at microscopic level between metal particles in the anode [4].

2. Experimental

2.1. Materials

Materials combining Cu or Cu–Ni with CeO_2, $Ce_{0.9}Gd_{0.1}O_{2-x}$ or $Ce_{0.8}Tb_{0.2}O_{2-y}$ were prepared by coprecipitation within reverse microemulsions. For this purpose, two reverse microemulsions, of similar characteristics concerning the volumes employed of organic (n-heptane) and aqueous phases as well as of surfactant (Triton X-100) and co-surfactant (1-hexanol), were prepared; details of the method can be found elsewhere [23]. The first one contained in its aqueous phase the dissolved (nitrate) salts of Ce, Gd, Tb, Cu or Ni while the second one contained in its aqueous phase a dissolved base (tetramethyl ammonium hydroxide or TMAH) which is employed as precipitating agent. Mixing both microemulsions produces the precipitation of the cations and after separation of the solid by centrifugation and decanting, the resulting solid is rinsed with methanol and dried for 24 h at 100 °C. The resulting material is then calcined under air initially at 500 °C during 2 h and finally at 950 °C during 2 h, employing relatively slow heating ramps of 2 min^{-1}. Samples with total metal loading of 40 wt.% (with 1/1 atomic ratios for bimetallic Cu–Ni systems) have been prepared. Similar microemulsion-precipitation methods were employed to prepare reference compounds with a final calcination being performed at 950 °C. Chemical analyses of the samples by ICP-AES demonstrated quantitative precipitation in any of the samples, the actual contents of any component being the same (within experimental error) as the nominal values employed. The samples will be denoted hereafter as M–C, M–CG and M–CT (with M = Cu or CuNi) depending on whether the support material is CeO_2, $Ce_{0.9}Gd_{0.1}O_{2-x}$ or $Ce_{0.8}Tb_{0.2}O_{2-y}$, respectively.

2.2. Techniques

Specific surface area (S_{BET}) determination was made from curves of adsorption/desorption of N_2 at 77 K over the samples outgassed at 140 °C using a Micromeritics ASAP 2100 equipment.

Powder XRD patterns of the samples were recorded on a Seifert XRD 3000P diffractometer using nickel-filtered Cu Kα radiation operating at 40 kV and 40 mA, using a 0.02° step size and 2 s counting time per point.

X-ray photoelectron spectra (XPS) were recorded with a Leybold-Heraeus spectrometer equipped with an EA-200 hemispherical electron multichannel analyzer (from Specs) and a 120 W, 30 mA Mg Kα X-ray source. The samples (0.2 mg) were slightly pressed into a small (4 mm × 4 mm) pellet and then mounted on the sample rod and introduced into the pretreatment chamber of the spectrometer where they were briefly outgassed and then moved into the ion-pumped analysis chamber where it was further outgassed until a pressure less than 2×10^{-9} Torr was attained (2–3 h). This low pressure was maintained during all the data acquisition by ion pumping of the chamber. After each treatment, XP spectra in the relevant energy windows were collected for 20–90 min, depending on the peak intensities, at a pass energy of 44 eV (1 eV = 1.602×10^{-19} J), which is typical of high resolution conditions. The intensities were estimated by calculating the integral of each peak after subtraction of an S-shaped Shirley-type background with the help of UNIFIT for Windows (version 3.2) software [24]; atomic ratios were then derived using the appropriate experimental sensitivity factors. All binding energies (BE) were referenced to the Ce(3d) u‴ line at 917.0 eV which, as we have previously shown [25], gives a value of 284.6 ± 0.1 eV for the adventitious graphitic C(1s) line.

Raman spectra were collected at room temperature using a Renishaw Dispersive System 1000 equipped with a cooled CCD detector and holographic Notch filter. The samples were excited with the red laser line (632.8 nm) and the spectral resolution was 3 cm^{-1}.

Temperature programmed reduction (TPR) tests under diluted dry methane (5% CH_4/He) were done in a quartz flow microreactor filled with about 500 mg of sample and employing 150 mL min^{-1} total flow. Heating ramps of 10 °C min^{-1} from 30 to 900 °C, maintaining finally this temperature for 2 h under the reactant mixture (enough in all cases for achieving stabilization of the reaction products), were used. Subsequently, the sample was cooled under the same flow and after extensive purging under He at 30 °C they were subjected to a temperature programmed oxidation (TPO) test under 5% O_2/He (using the same flow rate as for the TPR tests) up to 900 °C (10 °C min^{-1} ramp), keeping then this temperature until products

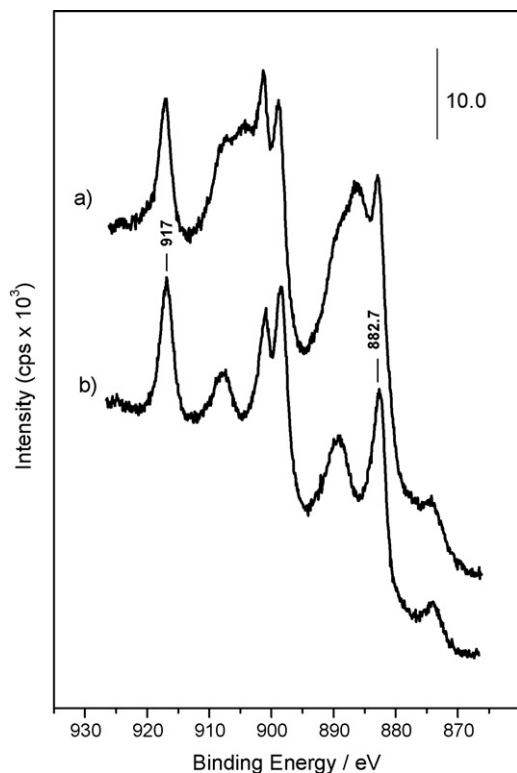**Fig. 1.** Ce(3d) XPS spectra of the samples subjected to CH_4-TPR tests up to 900 °C and exposed to atmospheric air. (a) CuNi–C and (b) CuNi–CT.

stabilization. Gases evolving from the reactor were analysed with a Pfeiffer Omnistar quadrupolar mass spectrometer.

Thermal expansion coefficients (TEC) were measured on an alumina dilatometer Linseis L75/1550, heating from room temperature to 750 °C at a rate of 5 °C min^{-1} both under air and 10% H$_2$/N$_2$. Prior to these measurements, samples were calcined for 2 h at 950 °C and cold-pressed into pellets (10 mm diameter and 0.9 mm thickness) at a pressure of 2 ton cm^{-2}.

The electrical conductivity of the materials (pressed into rectangular bars of 20 mm × 5 mm × 1.5 mm and pre-sintered under air at 950 °C for 2 h) was measured both in air and 10% H$_2$ by the four point DC method in the temperature range 200–750 °C. The electrical contacts were ensured with gold wire and a gold conductor paste (TR1531). A current load was applied by a Dual Output DC Power Supply (Agilent E3646A) and the potential drop recorded by a Digital Multimeter (Agilent E34401A). Supplementary scanning electron microscopy (SEM) analysis of the materials examined during these tests of electrical properties was done with a Hitachi-S-2500 microscopy.

3. Results and discussion

Specific surface area values obtained for all samples show a significant sintering upon calcining the samples at 950 °C (S_{BET} values between <0.5 and 1.6 m^2 g^{-1}). Nevertheless, –CG and –CT doped ceria samples generally show somewhat higher surface areas (with values higher than 1 m^2 g^{-1}) than the samples of the undoped-C series, thus revealing that doping with Gd or Tb helps to stabilize to some extent the systems towards thermal sintering, in agreement with previous findings [21,22].

The structural properties of the anode formulations either in the initial state after calcination at 950 °C or after having been subjected to TPR tests under diluted CH$_4$ was examined in a previous work on the basis of XRD results [22]. A summary of the main results is given hereafter for the readers' sake. The X-ray diffractograms of the initial samples calcined at 950 °C display mainly peaks due to the fluorite phase of either CeO$_2$- or Gd- or Tb-doped ceria [26,27].

Lattice parameters estimated from the diffractograms for this phase are of ca. 5.410, 5.416 and 5.390 Å for samples of the –C, –CG and –CT series, fairly independent on the presence of Cu or Ni in the formulation, consistent with the formation of the corresponding doped phases; in the case of the Tb-containing samples, this value indicates the presence of both Tb^{3+} and Tb^{4+} states, in agreement with previous analysis [27]. The average sizes of the fluorite crystals, determined from XRD linewidths using Scherrer's formula are of ca. 0.7, 0.6 and 0.5 μm for the calcined samples of the –C, –CG and –CT series, respectively, fairly consistent with the evolution of specific surface area values described above. In addition, the copper containing samples display the presence of tenorite CuO while in the case of bimetallic Cu–Ni systems the two metals appear as separate CuO and NiO oxide phases.

Important changes were detected in the X-ray diffractograms of the samples subjected to TPR under diluted methane up to 900 °C [22]. In first place, a reduced hexagonal Ce$_2$O$_3$ phase becomes stabilized under atmospheric air in the absence of doping with either Gd and Tb, while in the presence of these dopants the fluorite-type structure is retained, indicating that the latter are able to stabilize fluorite phases of the support, most likely related to a stabilization of a more highly oxidized state of Ce in the presence of trivalent dopants. This is consistent with the XPS results now obtained, illustrated in Fig. 1, which reveal the stabilization of a significant amount of reduced Ce^{3+} (mainly evidenced by the increase of peaks at ca. 904 and 886 eV [22,28]) in the absence of Tb, this being apparently independent on whether monometallic Cu or bimetallic CuNi systems are tested. Concerning the metal component, full reduction to the metallic state was detected by XRD in any of the cases after CH$_4$-TPR up to 900 °C and exposure to air [22]. In contrast to the phase separation of the CuO and NiO oxides observed in the initial calcined state for the CuNi bimetallic systems, those X-ray diffractograms of the three reduced CuNi-samples showed the formation of CuNi alloys (on the basis of the shift observed in the peaks with respect to positions expected for the pure metals), with no hint of separated phases being detected in any case. Interestingly, as judged from the XRD peak positions such alloy appears more enriched in copper for
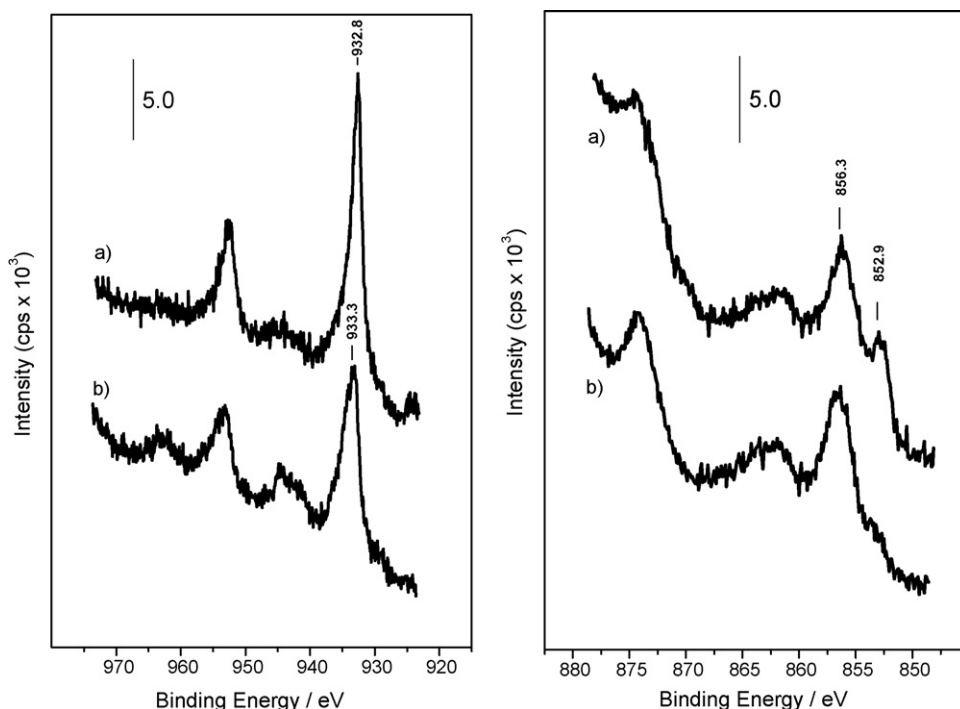

Fig. 2. Left: Cu(2p) XPS spectra of the samples subjected to CH$_4$-TPR tests up to 900 °C and exposed to atmospheric air. Right: the same for the Ni(2p) zone. (a) CuNi–C; (b) CuNi–CT.

the CG-based composite, which in turn suggests that this latter may present a surface enrichment in Ni for the alloy, while this effect does not appear for the C- or CT-based materials. On the other hand, XPS data now obtained provide a comparison of the state of the two metals in CuNi–C and CuNi–CT samples after the CH_4–TPR test up to 900 °C and exposure to atmospheric air at room temperature, Fig. 2. They show in the case of CuNi–C the presence of the metallic state for both metals, in agreement with XRD results, while, the spectra of CuNi–CT are consistent with the presence of oxidized states (Cu^{2+} and Ni^{2+}) for both metals: the main Cu(2p) peak is shifted to 933.3 eV and the satellite peak at ca. 944 eV increases, and the peak at 852.9 eV in the Ni(2p) spectrum strongly decreases. This indicates that, considering the XRD result that shows the formation of the CuNi alloy, surface oxidation occurs more extensively in the CuNi–CT case during exposure to atmospheric air at room temperature, likely forming passivating layers, as a consequence of the higher redox activity related to the higher oxygen mobility in the presence of the Tb dopant.

Concerning the analysis of redox/catalytic properties on the basis of CH_4-TPR testing, results in our former contribution compared the CO_2 evolution observed during such tests for the systems here examined [22]. A summary of main findings is provided hereafter while a representative picture is given in Fig. 3. Methane does not begin to react evolving CO_2 (which reflects full oxidation process, *vide infra*) in any of the cases until ca. 600 °C are attained. Interestingly, promoting effects for the reaction are observed for the highly sintered samples examined here in the case of the systems based on Ce–Gd or Ce–Tb mixed oxides, indicating a strong relevance of enhanced oxygen transport properties in the methane oxidation process [26]. On the other hand, comparison between the most active monometallic copper system (Cu–CG) and the bimetallic CuNi ones shows the significant contribution to the activity provided by the presence of nickel in the formulation, in consistency with the higher expected reactivity of this component towards methane [5–8]. As appreciated in Fig. 3, the methane oxidation activity among the bimetallic systems follows the order CuNi–CG > CuNi–CT > CuNi–C. In addition to the mentioned promoting effects of Gd or Tb on the oxidation process (similar to those observed for the monometallic copper systems [22]), the nature of the CuNi alloy formed in each case (which, as mentioned above, could be surface enriched in nickel in the case of the most active CuNi–CG system) can also play a significant role on the catalytic properties of these materials.

On the other hand, a complete quantitative analysis of all the gases evolving during these CH_4-TPR experiments gives important
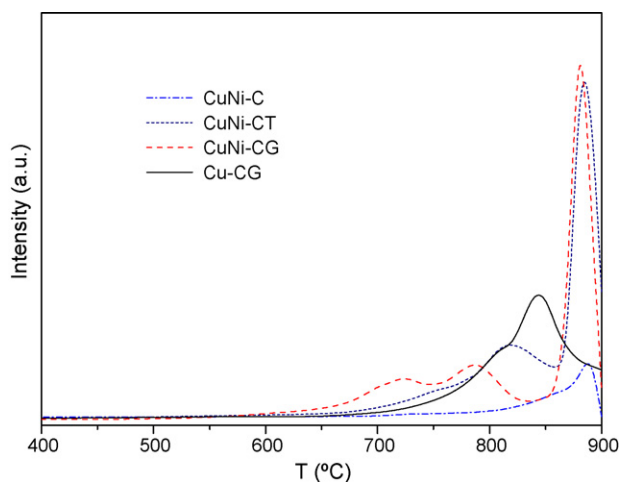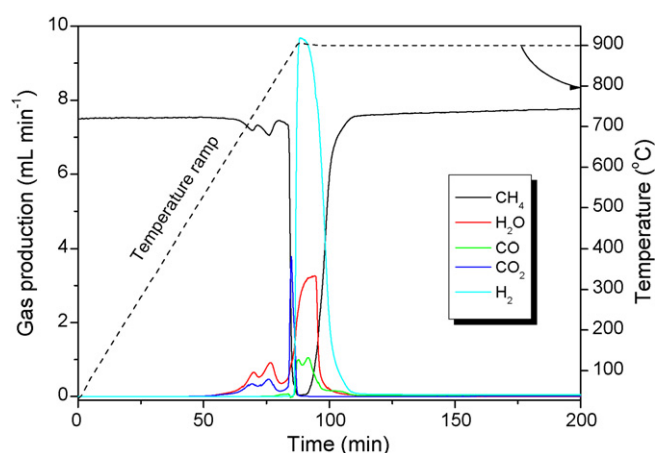

Fig. 4. Evolution of the indicated gases (according to quantification and appropriate correction of m/e = 2, 16, 18, 28 and 44 MS signals) during the CH_4-TPR test over the CuNi–CG sample.

hints on the processes taking place in the course of the test. As shown in Fig. 4, which displays the results of the test performed over the original oxidized CuNi–CG sample, the process of total methane oxidation ($CH_4 + 4O_{solid} \rightarrow CO_2 + 2H_2O$) prevails at lower temperature (between ca. 550 and 800 °C), at which reduction of Ni (and probably also of Cu) to the metal state has likely not yet been completed and thus carbon deposition is unlikely to be significant. This agrees with previous proposals suggesting that these systems could favour total oxidation under real SOFC operating conditions when oxygen transport is fast enough to provide oxygen to the methane molecules [4]. For temperatures approaching 900 °C at which the catalyst has certainly become reduced, partial oxidation processes ($CH_4 + O_{solid} \rightarrow CO + 2H_2$, $CH_4 + 2O_{solid} \rightarrow CO + 2H_2O$) are clearly revealed while probably methane cracking and generation of carbon deposits ($CH_4 \rightarrow C + 2H_2$) also occur at those temperatures.

TPO tests subsequent to the CH_4-TPR runs reveal the generation of carbon deposits upon interaction of the systems with methane, their magnitude being mainly a function of the presence of nickel in the catalysts. As displayed in Fig. 5, the amount of carbon deposited is appreciably higher in the presence of nickel, as expected from the mentioned higher reactivity of this latter towards methane [4–8], while it appears only residual in the monometallic copper systems. In this respect, it is also interesting the comparison between
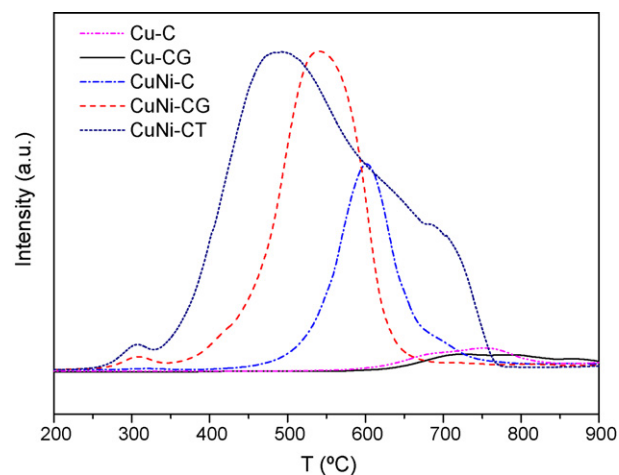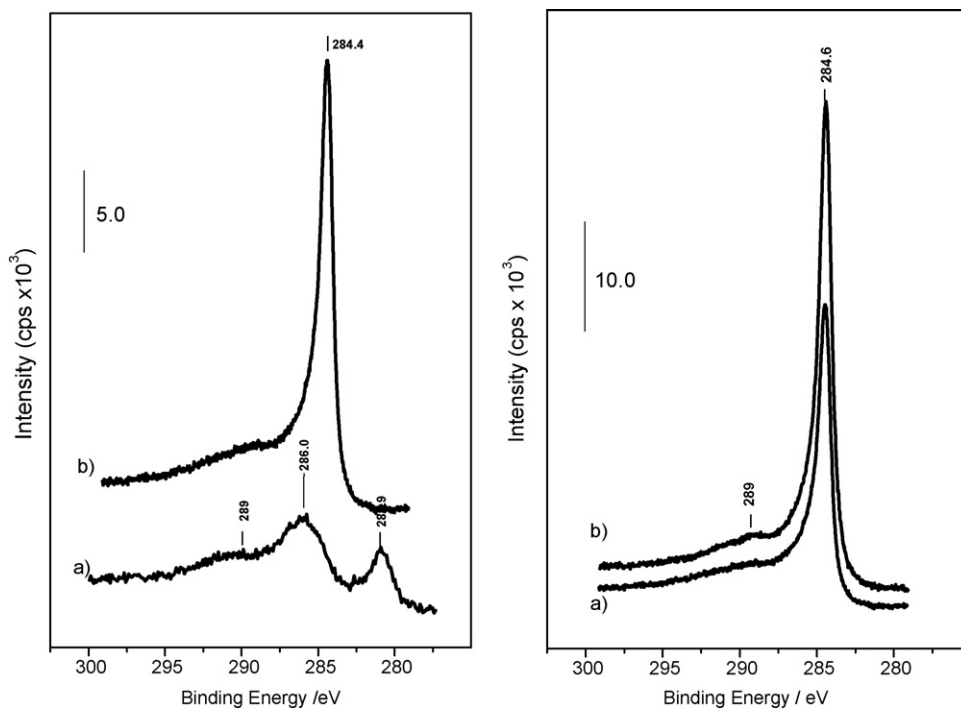

Fig. 3. Evolution of the m/e = 44 MS signal during CH_4-TPR tests over the indicated samples.

Fig. 5. Evolution of the m/e = 44 MS signal during TPO runs performed subsequently to CH_4-TPR tests over the indicated catalysts.

Fig. 6. C(1s) XPS spectra of the samples subjected to CH_4-TPR tests up to 900 °C. Left: (a) Cu–C and (b) CuNi–C. Right: (a) CuNi–C and (b) CuNi–CT.

CuNi–CG or CuNi–CT and CuNi–C, in which an appreciably higher amount of CO_2 is shown to evolve from the two former (Fig. 5). This correlates well with the generally higher activity towards methane shown by the systems including Gd or Tb dopants in the formulation. Our former contribution revealed in fact that only a residual amount of carbon appeared to be retained by the monometallic copper catalysts [22], although its nature, in contrast to carbon deposits formed in the presence of nickel and in correlation with TPO results displayed in Fig. 5, appeared to be related to very stable forms of carbon, likely in the form of carbide compounds. This has been evidenced by XPS, as displayed in Fig. 6. Thus, in the case of the Cu–C sample, besides the contribution at ca. 289 eV, due to the Ce(4s) photoemission, the spectrum displays a relatively weak peak at ca. 286.0 eV while a sharper peak at ca. 280.9 eV appears which is absent in the nickel-containing samples. Taking into account that the reference graphitic carbon would appear at ca. 284.6 eV, which is the main contribution detected in the case of CuNi–C or CuNi–CT samples, the weak signal (consider the mentioned overlapping) appearing at 286.0 eV may well belong to oxygen bonded –[CH_2]– polymeric species while the relatively strong B.E. shift of the sharp signal observed at ca. 280.9 eV in the sample Cu–C suggests that it must be associated to some carbide-like phase of the type C_yCe or C_yCe_xCu, by analogy to well known phases such as CW, CTi or CHf [28]. In turn, comparison between CuNi–C and CuNi–CT samples confirm the greater amount of graphitic-like deposits formed for the latter (Fig. 6), in agreement with TPO results.

Further hints on the formation and nature of the carbon deposits created upon interaction with CH_4 are provided by Raman results. In the case of the three bimetallic CuNi systems, the spectra display the formation of bands related to this type of species upon such interaction which are essentially constituted by two contributions at 1330 and 1582 cm^{-1} along with a shoulder at ca. 1620 cm^{-1}, as illustrated in Fig. 7. The band at 1582 cm^{-1} is characteristic of graphitic structures while the other contributions are related to less ordered carbonaceous structures [29,30]. In this sense, analysis of the ratio between the intensities of the bands

at 1330 cm^{-1} (so-called band D) and 1582 cm^{-1} (so-called band G) gives values of $I_D/I_G = 0.6$–0.8 and 0.5–1.1 (depending on the zone analysed) for CuNi–C and CuNi–CG, respectively, suggesting a more homogeneous nature for the carbon deposits formed in the former and the presence in the latter of a portion of highly disordered and unevenly distributed carbonaceous structures. This is in fair agreement with TPO results (Fig. 5) displaying a more irregular and wider shape in the profile observed for CuNi–CG while some of the deposits (most likely those with a higher degree of disorder) are burned at lower temperature in this catalyst. The results observed for the CuNi bimetallic samples contrasts with spectra for the monometallic copper samples in which no band in this zone is observed to form after subjecting the samples to CH_4-TPR tests, in agreement with the relatively low amount of carbon formed on these systems and/or its essentially carbidic character.
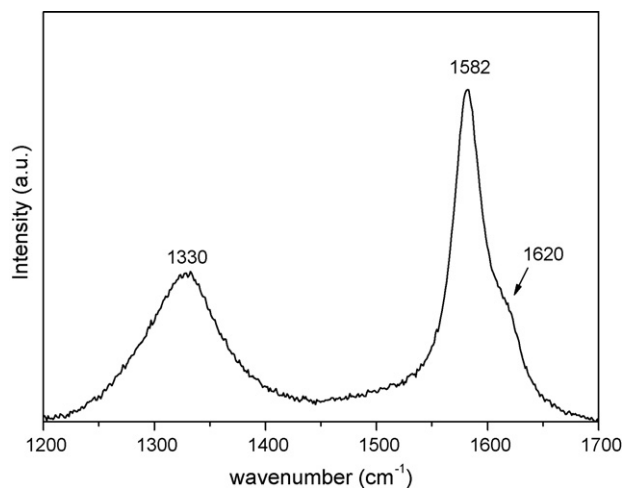
Fig. 7. Raman spectrum of CuNi–C after the CH_4-TPR test.
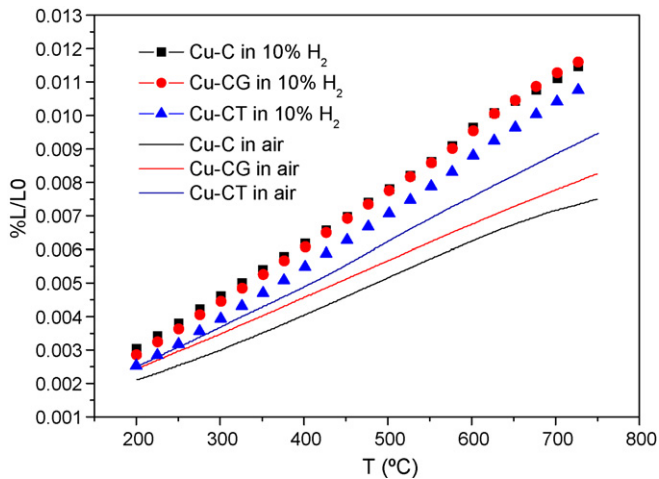
Fig. 8. Thermal expansion curves for monometallic systems in air and 10% H$_2$/N$_2$.
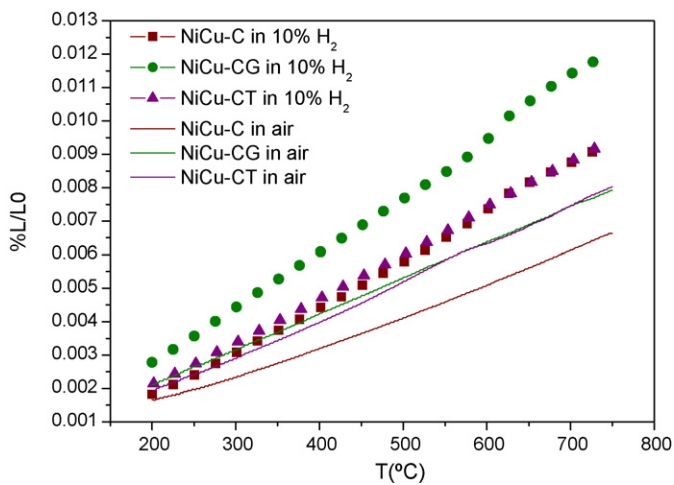

Fig. 9. The same as Fig. 8 for the bimetallic samples.

Concerning thermal expansion measurements, the influence of Gd or Tb doping of ceria in the expansion thermal coefficient was studied for both monometallic and bimetallic systems. The thermal expansion curves for monometallic and bimetallic samples, both in air and 10% H$_2$, in the temperature range from 200 to 750 °C are displayed in Figs. 8 and 9, respectively. The average thermal expansion coefficients for all compositions, obtained from the slope of the line in the temperature range 200–750 °C, are listed in Table 1. The TEC values are between 9.26×10^{-6} and 12.86×10^{-6} °C^{-1} under oxidizing atmosphere and between 13.49×10^{-6} and 16.87×10^{-6} °C^{-1} under H$_2$. These differences result form the combination of several factors. Thus, the partial replacement of Cu by Ni leads to lower TEC values in both air and 10% H$_2$/N$_2$. This could be due, in the reduced case, to the higher cohesive energy of nickel (that will influence in the same direction
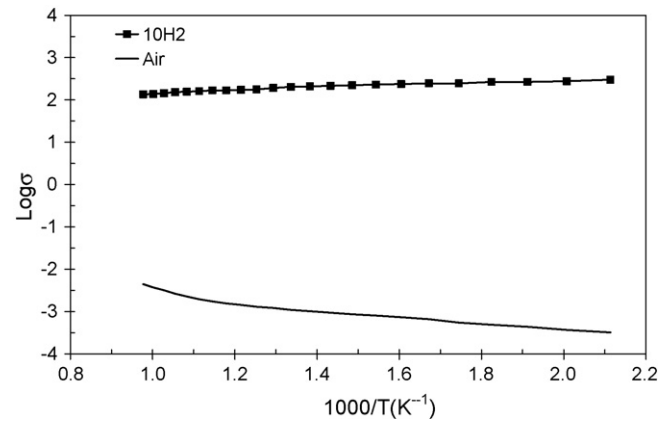

Fig. 10. Electrical conductivity of Cu–C sample in air and 10% H$_2$ as a function of temperature.

that of the alloy) than that of copper; and in the oxidized case, to a similar effect; although cohesive energies are not available, these are likely to be higher in the more compact NiO phase. Secondly, the achievement of higher TEC values in reducing atmosphere can be ascribed to the lower cohesive forces that result in the reduced lanthanide oxide phase (due to the decrease in both average cation charge and number of anions). Thirdly, the incorporation of Gd and Tb in the structure produces in most cases an increase in the TEC values, which may be attributed as well to the increase in the number of oxygen vacancies and the simultaneous decrease in average cation charge that occur upon substitution of Ce^{4+} by Gd^{3+} or Tb^{3+}. Comparing the effect of the two dopants, the TEC values obtained with Tb are higher in the oxidized samples and lower under reducing condition; this arises probably from a complex interplay between the higher dopant concentration of Tb (20 at.% for Tb and 10 at.% for Gd) and the differences in ionic radii between Gd^{3+}, Tb^{3+} and Tb^{4+}. In general, the TEC values obtained are close to those of 8YSZ, LSGM (La$_{0.9}$Sr$_{0.1}$Ga$_{0.8}$Mg$_{0.2}$O$_{3-\delta}$) and CGO (Ce$_{0.8}$Gd$_{0.2}$O$_{2-\delta}$) ($\approx 10.5 \times 10^{-6}$, 11.8×10^{-6} and 12.9×10^{-6} °C^{-1}, respectively), electrolytes commonly used in SOFC and IT-SOFC.

Concerning electrical conductivity measurements, Fig. 10 shows the results obtained for the Cu–C sample as a function of temperature in air and 10% H$_2$. Under air, copper exists in the form of CuO and the total conductivity of the composite results mainly from the ionic conduction of the oxides. Accordingly, the sample in air shows low conductivity (0.039 S/cm at 750 °C) and semiconductor behaviour, the conductivity increasing with increasing temperature. When the sample is reduced, the Cu cermet shows a considerably higher conductivity (135.3 S/cm at 750 °C) increasing by about 5 orders of magnitude. Therefore, when the CuO composite is reduced to metallic copper metal (as confirmed by XRD), the metallic particles apparently tend to form a continuous network. In this case, the electrical conductivity mainly depends on the electronic conduction of copper metal. As expected for a metal dominated system, electrical conductivity decreases a little with increasing temperature. Table 2 summarizes the results of electrical conductivity for

Table 1
TEC values of monometallic and bimetallic samples in air and 10% H$_2$.

Sample	TEC (°C^{-1}) in air	TEC (°C^{-1}) in 10% H$_2$
Cu–C	10.38×10^{-6}	16.30×10^{-6}
Cu–CG	10.74×10^{-6}	16.87×10^{-6}
Cu–CT	12.86×10^{-6}	15.99×10^{-6}
CuNi–C	9.26×10^{-6}	14.15×10^{-6}
CuNi–CG	10.66×10^{-6}	15.78×10^{-6}
CuNi–CT	11.28×10^{-6}	13.49×10^{-6}

Table 2
Electrical conductivity of Cu–C, Cu–CG, CuNi–C, CuNi–CG in air and 10% H$_2$ at 750 °C.

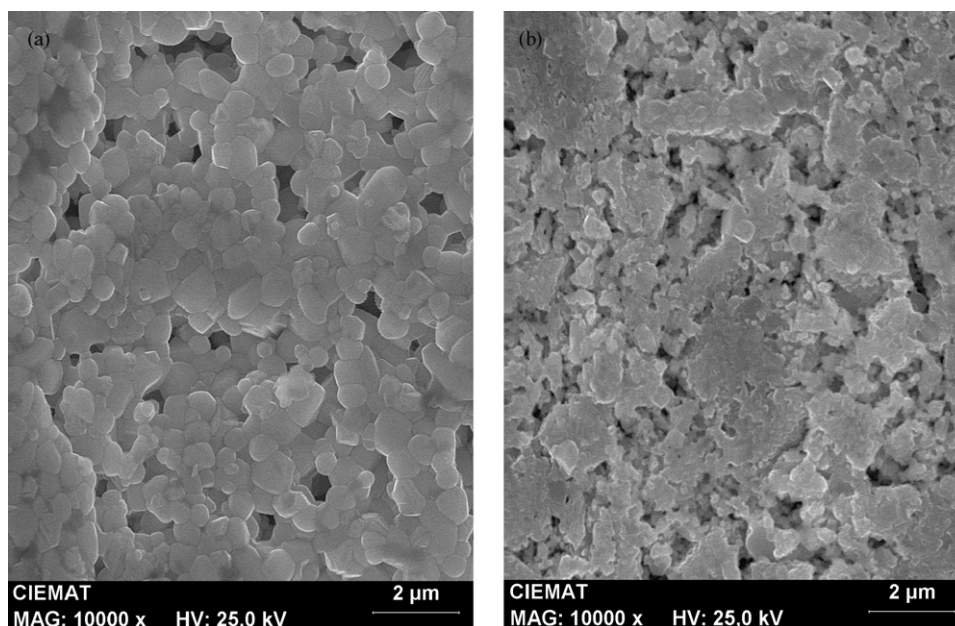| Electrical conductivity (S cm^{-1})		
Sample	Air	10% H$_2$
Cu–C	0.039	135.3
Cu–CG	0.004	34.1
NiCu–C	0.052	24.8
NiCu–CG	0.015	2.44

Fig. 11. SEM micrographs of CuNi–C (a) and CuNi–CG (b).

four compositions studied at 750 °C under air and 10% H_2. Under reduction conditions, the bimetallic CuNi samples have a conductivity one order of magnitude lower in comparison with the Ni-free analogous sample. This could be due to a higher electrical conductivity of copper in comparison with nickel, as well as to the higher sinterability of copper [31]. On the other hand, under oxidizing conditions the composites with nickel and copper oxides show a lower electrical conductivity. This suggests a higher conductivity of NiO than CuO. However, doping of Ce with Gd decreases the electrical conductivity of samples, which can be most likely due to microstructural changes (as detected by SEM, Fig. 11), which would affect interparticle resistivity and be the most relevant factor, rather than intraparticle conductivity (expected to be higher upon Gd doping [26]). In this sense, it can be noted that this type of discrepancies are typical in comparisons of transport properties evaluated by conductivity measurements vs. tracer diffusion methods [32].

4. Conclusions

Different materials involving combinations of copper–nickel (compared with reference monometallic copper) with either ceria or Ce–Gd and Ce–Tb mixed oxides have been examined with respect to their structural and redox/catalytic properties towards oxidation of methane in the context of their potential application as anodes of SOFC for direct oxidation of hydrocarbons. CH_4-TPR results reveal important differences as a function of the presence of Ni as well as Gd and Tb in the systems. While, as expected, the presence of Ni appreciably enhance the methane reactivity, the doping of ceria by Gd or Tb is shown to be also generally beneficial for such reactivity as a consequence of the modifications induced in the catalytic/redox or transport properties of the materials. This suggests that the more complex bimetallic Cu–Ni formulations combined with doped ceria can offer higher efficiency in direct hydrocarbon oxidation SOFC operation. Differences in the methane reactivity as a function of the redox state of the catalyst are also revealed. As expected, the full oxidation process is favoured when the systems are oxidized while partial oxidation and/or methane cracking processes leading to carbon deposition prevail upon reduction of the materials during the course of thermal interaction with methane. The nature of such carbon deposits has been analysed by TPO, XPS and Raman, and confirm that their amount increases in the presence of nickel and apparently depend on the absence/presence of nickel in the formulation as well as on the presence of Gd or Tb dopants in the fluorite phase of the supports. Carbon deposits are formed in considerably lower amount in the copper only systems and apparently form very stable deposits in the form of carbidic compounds, in contrast to carbon deposits formed in the presence of nickel which are essentially of a graphitic nature as well as disordered carbonaceous structures. The beneficial effects on the methane activity observed in the presence of Tb or Gd dopants in ceria can be related to the stabilization of the fluorite phase in them, even after strong reduction under methane, which could also prevent the generation of carbidic alloys and facilitate also the oxidation at relatively low temperature of the carbonaceous deposits formed upon interaction with methane. The analysis of thermal expansion coefficients of the anodic formulations reveal, as expected, higher values under reducing conditions, appearing in any case in ranges close to those observed for typical electrolytes usually utilized in SOFCs and IT-SOFCs like 8YSZ, LSGM and CGO). Electrical conductivity of the various anodic formulations under air basically results from the oxygen ion conductivity of doped material while under reducing conditions, the conductivity mainly roots in the electronic conduction of copper and nickel metals, generally decreasing the value upon incorporation of Ni- and Gd-doping, mainly as a consequence of microstructural differences between the samples.

References

[1] B.C.H. Steele, A. Heinzel, Nature 414 (2001) 345.
[2] B.C.H. Steele, J. Mater. Sci. 36 (2001) 1053.
[3] J.M. Ralph, A.C. Schoeler, M. Krumpelt, J. Mater. Sci. 36 (2001) 1161.
[4] S. McIntosh, R.J. Gorte, Chem. Rev. 104 (2004) 4845.
[5] G.M. Crosbie, E.P. Murray, D.R. Bauer, H. Kim, S. Park, J.M. Vohs, R.J. Gorte, SAE paper 2001-01-2545. (2001).
[6] E.P. Murray, T. Tsai, S.A. Barnett, Nature 400 (1999) 649.
[7] S. Park, R.J. Gorte, J.M. Vohs, Appl. Catal. A 200 (2000) 55.
[8] A.-L. Sauvet, J. Fouletier, J. Power Source 101 (2001) 259.
[9] S. Park, R. Craciun, J.M. Vohs, R.J. Gorte, J. Electrochem. Soc. 146 (1999) 3603.
[10] R. Craciun, S. Park, R.J. Gorte, J.M. Vohs, C. Wang, W.L. Worrell, J. Electrochem. Soc. 146 (1999) 4019.
[11] S. Park, J.M. Vohs, R.J. Gorte, Nature 404 (2000) 265.
[12] R.J. Gorte, S. Park, J.M. Vohs, C. Wang, Adv. Mater. 12 (2000) 1465.
[13] H. Kim, S. Park, J.M. Vohs, R.J. Gorte, J. Electrochem. Soc. 148 (2001) A693.
[14] R.J. Gorte, J.M. Vohs, R. Craciun. Patents WO 00/52780; US 2001/0029231 A1; US 2001/0053471 A1.
[15] R.J. Gorte, H. Kim, J.M. Vohs, J. Power Source 106 (2002) 10.
[16] R.J. Gorte, J.M. Vohs, J. Catal. 216 (2003) 477.
[17] S. Jung, C. Lu, H. He, K. Ahn, R.J. Gorte, J.M. Vohs, J. Power Source 154 (2006) 42.
[18] C. Sun, U. Stimming, J. Power Source 171 (2007) 247.
[19] Z. Xie, W. Zhu, B. Zhu, C. Xia, Electrochim. Acta 51 (2006) 3052.
[20] M. Fernández-García, A. Martínez-Arias, J.C. Hanson, J.A. Rodriguez, Chem. Rev. 104 (2004) 4063.
[21] A. Martínez-Arias, A.B. Hungría, M. Fernández-García, A. Iglesias-Juez, J.C. Conesa, G.C. Mather, G. Munuera, J. Power Source 151 (2005) 43.
[22] A. Hornés, D. Gamarra, G. Munuera, J.C. Conesa, A. Martínez-Arias, J. Power Source 169 (2007) 9.
[23] A. Martínez-Arias, M. Fernández-García, V. Ballesteros, L.N. Salamanca, J.C. Conesa, C. Otero, J. Soria, Langmuir 15 (1999) 4796.
[24] R. Hesse, T. Chassé, R. Szargan, Fresenius J. Anal. Chem. 365 (1999) 48.
[25] A. Martínez-Arias, M. Fernández-García, A.B. Hungría, J.C. Conesa, G. Munuera, J. Phys. Chem. B 107 (2003) 2667.
[26] A. Trovarelli, in: A. Trovarelli (Ed.), Catalysis by Ceria and Related Materials, Imperial College Press, 2002, p. 15 (Chapter 2).
[27] A.B. Hungría, A. Martínez-Arias, M. Fernández-García, A. Iglesias-Juez, A. Guerrero-Ruiz, J.J. Calvino, J.C. Conesa, J. Soria, Chem. Mater. 15 (2003) 4309.
[28] J.P. Holgado, R. Alvarez, G. Munuera, Appl. Surf. Sci. 161 (2000) 301.
[29] S.C. Ray, C.W. Pao, H.M. Tsai, B. Base, J.W. Chiou, W.F. Pong, D. Dasgupta, Carbon 44 (2006) 1982.
[30] R.J. Nemanich, S.A. Solin, Phys. Rev. B 20 (1979) 392.
[31] E.V. Tsipis, et al., J. Eur. Ceram. Soc. 25 (1995) 2623.
[32] G.C. Mather, A. Martínez-Arias, in: J.A. Rodriguez, M. Fernández-García (Eds.), Synthesis, Properties and Applications of Oxide Nanomaterials, John Wiley & Sons, New Jersey, 2007, pp. 353–378 (Chapter 13).